World Scientific
www.worldscientific.com

DENOISING AND ENHANCEMENT OF MAMMOGRAPHIC IMAGES UNDER THE ASSUMPTION OF HETEROSCEDASTIC ADDITIVE NOISE BY AN OPTIMAL SUBBAND THRESHOLDING

ARIANNA MENCATTINI[*], GIULIA RABOTTINO[†],
MARCELLO SALMERI[‡] and ROBERTO LOJACONO[§]

Department of Electronic Engineering, University of Rome "Tor Vergata"
Via del Politecnico 1, 00133 Rome, Italy
[*]*mencattini@ing.uniroma2.it*
[†]*rabottino@ing.uniroma2.it*
[‡]*salmeri@ing.uniroma2.it*
[§]*lojacono@ing.uniroma2.it*

BERARDINO SCIUNZI

Department of Mathematics, University of Calabria
Via Pietro Bucci, 87036 Arcavacata di Rende (CS), Italy
sciunzi@mat.unical.it

Mammographic images suffer from low contrast and signal dependent noise, and a very small size of tumoral signs is not easily detected, especially for an early diagnosis of breast cancer. In this context, many methods proposed in literature fail for lack of generality. In particular, too weak assumptions on the noise model, e.g., stationary normal additive noise, and an inaccurate choice of the wavelet family that is applied, can lead to an information loss, noise emphasizing, unacceptable enhancement results, or in turn an unwanted distortion of the original image aspect. In this paper, we consider an optimal wavelet thresholding, in the context of Discrete Dyadic Wavelet Transforms, by directly relating all the parameters involved in both denoising and contrast enhancement to signal dependent noise variance (estimated by a robust algorithm) and to the size of cancer signs. Moreover, by performing a reconstruction from a zero-approximation in conjunction with a Gaussian smoothing filter, we are able to extract the background and the foreground of the image separately, as to compute suitable contrast improvement indexes. The whole procedure will be tested on high resolution X-ray mammographic images and compared with other techniques. Anyway, the visual assessment of the results by an expert radiologist will be also considered as a subjective evaluation.

Keywords: Discrete Dyadic Wavelet Transform; heteroscedastic additive noise; adaptive thresholding.

AMS Subject Classification: 42C40, 60H40

1. Introduction and Statement of Main Results

In this paper, we deal with the denoising and contrast improvement of low contrast images. We consider a general noise model given by

$$I(n, m) = I_0(n, m) + \tilde{I}(n, m) = I_0(n, m) + \eta(n, m) \cdot \sigma(I_0(n, m)), \quad (1.1)$$

where $n = 1, \ldots, N$, $m = 1, \ldots, M$, $I_0(n, m)$ is a $N \times M$ matrix representing a low contrast noise free image, $\eta(n, m)$ is a Wide Sense Stationary (WSS) Gaussian random process with zero mean and unitary variance and $\sigma(I_0(n, m)) : [0, 1] \to \mathbb{R}$ denotes the intensity-dependent standard deviation of random process $\tilde{I}(n, m)$. The scope of our work is to perform denoising and contrast enhancement of $I(n, m)$, under the following hypotheses: noise is assumed to be heteroscedastic (i.e. with nonconstant variance), images have low contrast and very small details, which are commonly encountered features in medical images such as, for example, X-ray mammographic images.[1] In fact, in this context the acquisition and formation processes cause noise heteroscedasticity that can mask small details, while the similar absorption characteristics of normal glandular tissue and tumoral lesions cause a very low local contrast, thus making the early diagnosis of breast cancer a nontrivial task. According to AIRC (Italian Association on Cancer Research) and ACS (American Cancer Society), radiologists miss out 10–20% of lesions during diagnosis, so image quality improvement represents a key issue in every Computer Aided Diagnosis System (CADx). Moreover, cancer signs usually have various shape, dimension, and distribution in the images. For example, in mammographic images, cancer signs can be classified into microcalcifications, where tiny deposits of calcium appear as small bright spots with a mean diameter in the range [0.1–1] mm which are relevant if distributed in cluster and massive lesions that are space occupying lesions, with a mean luminance much more similar to glandular tissue and a mean diameter in the range [0.3–40] mm. In this paper, we consider mainly region containing microcalcifications, that represent the most difficult signs to be detected by every Computer Assisted Diagnosis system (CADx) owing to the small size and the high similarity to noise.

Actually, in the last 20 years, many approaches have been applied to deal with the contrast enhancement of medical images (we refer to Ref. 6 and references therein), including filtering methods,[32] global and local thresholding methods,[14,9] histogram equalization,[21] unsharp masking,[4] region-based approach,[36] morphological operators,[27,28] wavelet transform,[50,22] and fuzzy logic approaches.[5] Basically, all these methods deal with contrast manipulation, noise reduction, background removal, edge detection, and smoothing. The approaches can be roughly classified into three categories: contrast stretching techniques, region-based enhancement techniques, and feature-based approaches.

The first group includes *unsharp masking* that improves contrast by subtracting a smoothed version of the image to the image itself and adaptive neighborhood processing[9] that uses first derivative filters (Sobel) and local statistical properties. However, this class of methods changes the final image or emphasizes noise.

The second group uses modified versions of region growing algorithm to grow regions around a seed pixel. In this way, a detailed reconstruction of objects is achieved, also in low contrast images. However, this kind of approach is successfully applied to the segmentation of large objects, such as massive lesions. On the contrary, this technique is not suitable for the denoising of small spots.

Finally, the third group includes *multiscale approaches* by wavelet transform,[25,17,38,42] B-spline function,[44] decimated wavelet transform,[48,49] undecimated biorthogonal transform,[43,45] fractal[28,27] and morphological analysis.[47] The latter two methods are used especially in strongly low contrast images, where the dense tissue reduces the visibility of microcalcifications. On the contrary, the wavelet approaches can preserve the shape of details (microcalcifications or the boundary of a tumoral mass) better than morphological operators. Therefore, despite of a growing complexity in the implementation of the methods and in the tuning of the parameters, wavelet transform represents one of the most effective approaches for the contrast enhancement of mammographic images, emphasizing small details, and reducing noise.

In this context, many wavelet thresholding techniques have been investigated. Some methods[19,40] evaluate the correlation between wavelet coefficients at different scale, as to identify noisy pixel (showing no correlation) and signal pixel (high correlation). Unfortunately, for a low number of levels and low noise, this approach fails while detecting microcalcifications. Other methods[11,10,23,7,18] select the thresholds for denoising directly by evaluating some statistical properties of the noise, or iteratively.[2] In particular, in Ref. 10, the authors suggest to use the robust estimator MAD (Median Absolute Deviation) to compute noise variance at each level, in a orthogonal wavelet transforms framework. The same work has then been extended in Ref. 20 by considering data affected by correlated noise in orthogonal wavelet framework and in Ref. 3 by assuming additive Gaussian noise in translation invariant DWT framework. Unfortunately, in this setting the assumption of a signal-independent, Gaussian, and homoscedastic noise and the choice of a decimated family of wavelets appear not suitable for many real-world images, such as medical images. In particular, it has been shown[23] that ultrasound, X-ray, and MRI images both are corrupted by a mixture of noise contributions. Moreover, it is well known that translation invariant undecimated wavelets, such as Discrete Dyadic Wavelet Transforms (DDWT), preserve much more information than classical orthogonal wavelet transforms, while reducing noise and improving contrast. In this paper, we exploit DDWT[30] to deal with the case of a signal-dependent noise contribution modeled in (1.1).

We take into account the following critical aspects:

— heteroscedasticity of noise modeled by (1.1) and represented by an additive Gaussian noise with a signal-dependent noise variance,
— very low local contrast and a poor visual discrimination between details and background tissue,
— very small size of details to be enhanced,

and requirements

— need of a translation invariant and undecimated wavelet transform (DDWT) to avoid geometric distortion in the images and loss of details,
— need of very high performance, in terms of computational time,
— need of preserving as much as possible the aspect of the original image, while enhancing details. This topic is crucial for helping radiologists in the diagnosis of cancer signs.

The algorithm we propose can be summarized in the following steps.

(i) Estimate the noise variance of $I(n, m)$ in (1.1) by applying a modified version of the algorithm described in Refs. 15 and 35, suitable in the case of heteroscedastic signal dependent noise. This step provides the estimation $\hat{\sigma}(\hat{I}(n, m))$ of the noise variance $\sigma^2(I_0)$ versus intensity value $\hat{I}(n, m)$ where $\hat{I}(n, m)$ is a preliminary estimation of $I_0(n, m)$ obtained by applying a smoothing filter to $I(n, m)$. Actually, we do not assume a direct dependence of the noise variance on the spatial locations. A preliminary investigation of a more general noise model with a spatial dependent noise variance can be found in Ref. 33.

(ii) Manually extract from the original image a suspicious Region of Interest (ROI) that could contain small cancer signs.

(iii) Perform wavelet decomposition by DDWT in $D = 3$ levels by applying gradient filters.

(iv) Apply wavelet thresholding for denoising, using $\hat{\sigma}(\hat{I}(n, m))$, and relate it to noise variance in each subband by energy evaluation of filters implementing DDWT. In this step, Theorem 1.1 will be fundamental since it will allow a fast implementation under suitable assumptions validated by simulation results.

(v) Apply again gradient filters so that a Laplacian is globally performed through steps (iii) to (v).

(vi) Perform enhancement by wavelet thresholding using considerations similar to those of step (iv) for the threshold selection. A new gain selection is also implemented by relating the gain to the mean size of cancer signs. In particular, the thresholding we implement for the enhancement is slightly different from the classical one since we make the following assumption: higher coefficients are related to details to be enhanced while lower ones reasonably represent very low contrast small spots related to noise or structures belonging to the tissue that have not been modified by denoising. This hypothesis is supported by the fact that details we are interested in, i.e. microcalcifications, have a medium contrast.

(vii) Extract separately background (glandular tissue) and foreground (cancer signs in our case) by performing a reconstruction from zero-approximation in conjunction with a Gaussian smoothing filter. As noted in Sec. 3, this procedure will allow us to perform a selective processing of foreground and

background and consequently the performance optimization of the global procedure.

(viii) Recover the final enhanced image by a suitable superimposition of background and foreground extracted at step (vii).

While introducing our approach, for the reader's convenience, we will also recall the main properties of DDWT.

1.1. *Wavelet thresholding in DDWT*

With respect to the DDWT firstly introduced by Mallat,[29–31] which represents a translation invariant and redundant representation, we consider the particular subclass of DDWT based on the so-called *Spline Dyadic Wavelets* since the scaling function $\phi(x)$ is a box spline function whose Fourier transform is given by $\Phi(\omega) = (\sin(\omega/2)/(\omega/2))^{z+1}e^{(-\iota\varepsilon\omega/2)}$ (where z is an integer and if $\varepsilon = 1$ z is even and zero otherwise). The filters banks for decomposition and reconstruction are shown in Figs. 1 and 2 where filters H, G, L and K in the Fourier domain are given by

$$H(\omega_q) = e^{\iota\omega_q s_1} \cos^{p+1}\left(\frac{\omega_q}{2}\right), \quad G(\omega_q) = e^{\iota\omega_q s_2}\left(2\iota\sin\left(\frac{\omega_q}{2}\right)\right)^r, \qquad (1.2)$$

$$K(\omega_q) = \frac{(1 - |H(\omega_q)|^2)}{G(\omega_q)}, \qquad L(\omega_q) = \frac{(1 + |H(\omega_q)|^2)}{2} \qquad (1.3)$$
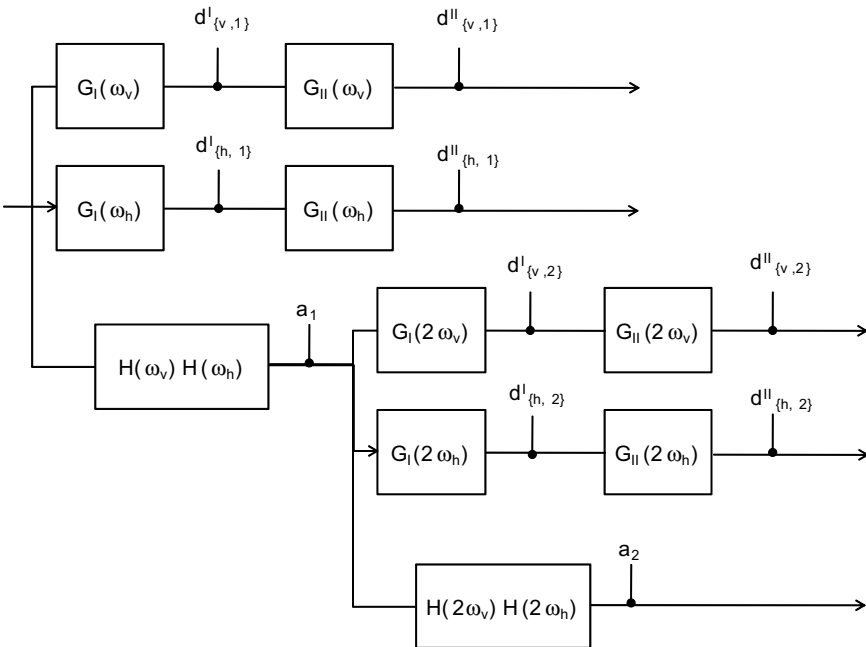

Fig. 1.   Filter bank implementation of DDWT decomposition in two-dimensional case.
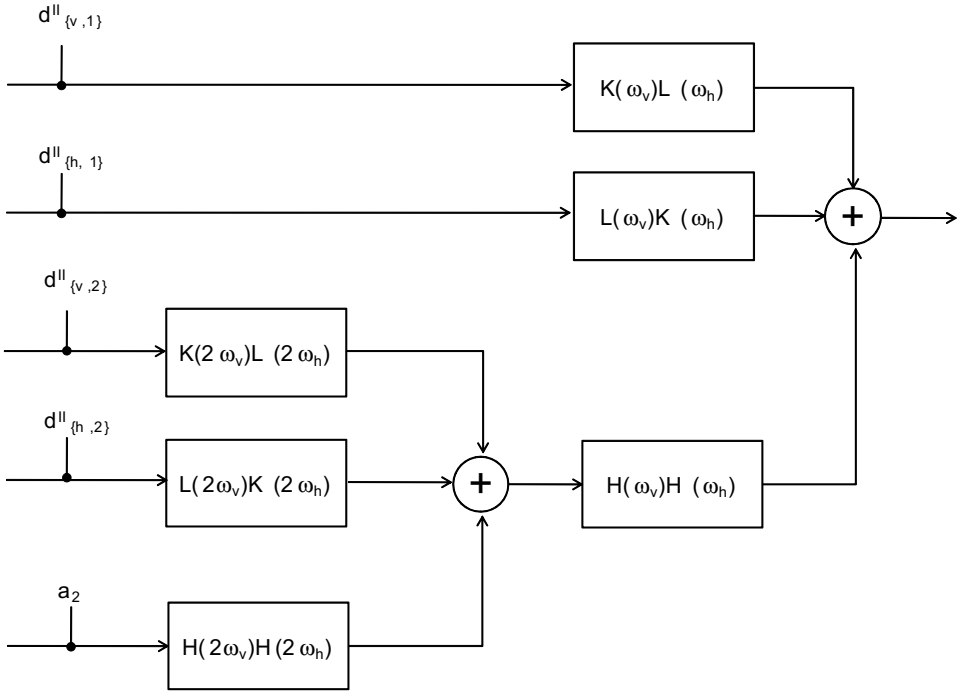
Fig. 2.   Filter bank implementation of DDWT reconstruction in two-dimensional case.

with $p \in \mathbb{N}$, $s_1 = \frac{1}{2}((p+1) \bmod 2)$, $r \in \{1,2\}$, $s_2 = \frac{1}{2}(r \bmod 2)$, $q \in \{v,h\}$, where the notations ω_v and ω_h mean that the filters are applied to the rows and the columns of the input image respectively owing to the separability of filters implementing the DDWT. Note that, in the two-dimensional case we have vertical and horizontal detail coefficients at level l that we will denote in the following as $d^o_{q,l}$ with $q \in \{v,h\}$, $o \in \{I, II\}$ at level l. This paper deals, in particular, with the case $p = 1$, $r = 2$ in (1.1). It is well known that this choice is greatly suitable to perform image enhancement (see Ref. 13 and references therein). In order to perform denoising, the filter $G(\omega_q)$, $q \in \{v,h\}$ is splitted into two cascaded gradient filters[13,46] (see Fig. 1), denoted as $G_I(\omega_q)$ and $G_{II}(\omega_q)$, given by $e^{-\iota \omega_q/2}(2\iota \sin(\omega_q/2))$ and $e^{\iota \omega_q/2}(2\iota \sin(\omega_q/2))$ respectively, and denoising is applied after $G_I(\omega_q)$. This approach improves denoising performance, since the Signal-to-Noise Ratio (SNR) is higher after G_I than after G_{II}. Nevertheless, the enhancement step is better performed after G_{II} as said before. The splitting we perform is a crucial point since it allows us to differentiate the actions we perform. Owing to the typical luminance values of the details to be enhanced, to their similarity in size with noise, and finally to their low contrast, denoising and enhancement performance are optimized by applying the splitting of the Laplacian filters into two gradient filters.

Consider now only the decomposition part shown in Fig. 1. Then, the transfer functions of filters at a generic level l are given by

$$
\begin{cases}
G_l(\omega_q) = G(2^{l-1}\omega_q) = -4\sin^2\left(\dfrac{2^{l-1}\omega_q}{2}\right) \\
\qquad = G_{l,I}(\omega_q) \cdot G_{l,II}(\omega_q) \\
H_l(\omega_q) = H(2^{l-1}\omega_q) = \cos^2\left(2^{l-1}\dfrac{\omega_v}{2}\right)
\end{cases}
\tag{1.4}
$$

with $l = 1, \ldots, D$, $q \in \{v, h\}$ and splitted filters given by

$$
\begin{cases}
G_{l,I}(\omega_q) = e^{-\frac{2^{l-1}\iota\omega_q}{2}} 2\iota \sin\left(\dfrac{\omega_q}{2}\right) \\
G_{l,II}(\omega_q) = e^{\frac{2^{l-1}\iota\omega_q}{2}} 2\iota \sin\left(\dfrac{\omega_q}{2}\right)
\end{cases}
\tag{1.5}
$$

with $l = 1, \ldots, D$ and $q \in \{v, h\}$. Consider again scheme in Fig. 1 and let us denote with $G_l^T(\omega_q)$ and $H_l^T(\omega_q)$ the cascaded transfer functions up to level l having the noisy image as input and $d_{q,l}^o$ and a_l as outputs respectively, with $q \in \{v, h\}$, $o \in \{I, II\}$, $l = 1, \ldots, D$. Then, we have

$$
\begin{cases}
G_l^T(\omega_q) = H_1(\omega_q) \cdots H_{l-1}(\omega_q) \cdot G_l(\omega_q), \\
H_l^T(\omega_q) = H_1(\omega_q) \cdots H_{l-1}(\omega_q) \cdot H_l(\omega_q).
\end{cases}
\tag{1.6}
$$

Equation (1.6) holds either if $G_l(\omega_q) \equiv G_{l,I}(\omega_q)$ and if $G_l(\omega_q) \equiv G_{l,II}(\omega_q)$. In the two cases, we get $|G_{l,I}^T|$ and $|G_{l,II}^T|$, respectively. Following above observations, the whole denoising and enhancement scheme is shown in Fig. 3. The denoising operator $D(\cdot)$ is implemented by a *soft-threshold function*,[10] defined by

$$
D(x) = \begin{cases}
\text{sign}(x)(|x| - T_{\text{noise}}) & |x| \geq T_{\text{noise}}, \\
0 & \text{otherwise},
\end{cases}
\tag{1.7}
$$

where T_{noise} is the denoising threshold to be suitably set. Soft-thresholding is usually preferred to hard-thresholding[12] since the use of a continuous operator $D(x)$ instead
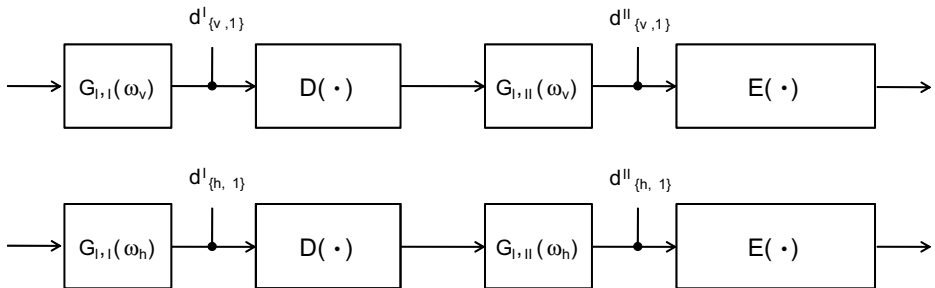

Fig. 3. Splitting of the second-order derivative filters (level l is shown) for denoising and contrast enhancement.

of a discontinuous one avoids the introduction of artifacts in the wavelet coefficients. This issue is crucial in critical applications such as medical image processing.

It is well known that T_{noise} is mainly related to noise variance. Consequently, extending results in Refs. 11 and 26 in case of heteroscedastic additive noise, we use the following threshold model[a]:

$$T_{\text{noise}}(l, \hat{I}(n, m)) = \hat{\sigma}_{d^I}(q, l, I(n, m))\sqrt{2\log(N \cdot M)},$$
$$n = 1, \ldots, N, \quad m = 1, \ldots, M, \tag{1.8}$$

where $N \times M$ is the size of digital image $I(n, m)$, $q \in \{v, h\}$, for each level $l = 1, \ldots, D$, and $\hat{\sigma}_{d^I}(q, l, I(n, m))$ is the estimation of the noise standard deviation performed on details coefficients $d_{q,l}^I$ at level l. Note that thresholds in (1.8) depend on the intensity, owing to term $\hat{\sigma}_{d^I}(q, l, I(n, m))$, since we assumed heteroscedastic noise in the image $I(n, m)$. Later, we will show in details this relationship. At this point, we recall a preliminary result, proved in Ref. 34, that represents the starting point of this paper. In particular, in Ref. 34 it was proved that given a two-dimensional WSS homoscedastic random process $x(n, m)$, input of filter bank in Fig. 1, and consider relations (1.4) and (1.6), then, by symmetry of the filter bank in Fig. 1, the constant variance of process $d_{q,l}^I$, denoted as $\sigma_{d^I}^2(q, l)$, where $q = \{v, h\}$ and $l = 1, \ldots, D$, is given by

$$\sigma_{d^I}^2(q, l) = \sigma_x^2 \frac{(2^{2(l-1)} + 1)(2^{2l-1} + 1)}{3 \cdot 2^{6(l-1)}} \tag{1.9}$$

where σ_x^2 is the constant variance of the random process $x(n, m)$.

This result models the propagation of noise variance throughout wavelet levels for DDWT under the assumption of additive homoscedastic noise model with a constant noise variance σ_x^2.

In this paper, we consider the case of a heteroscedastic intensity-dependent additive noise model whose variance can be represented by $\sigma^2(I_0(n, m))$ referring to (1.1).

Let us denote with $\hat{\sigma}^2(\hat{I})$ the estimation of the noise variance in the image $I(n, m)$. Then, we introduce the local variation $V_S[\hat{\sigma}^2(\hat{I})]$ defined by

$$V_1[\hat{\sigma}^2(\hat{I})] \equiv \sup_{n,m} |\hat{\sigma}^2(\hat{I}(n-1, m-1)) - \hat{\sigma}^2(\hat{I}(n, m))|,$$

$$V_2[\hat{\sigma}^2(\hat{I})] \equiv \sup_{\substack{n,m \\ (k,j)\in\{1,2\}\times\{1,2\}}} |\hat{\sigma}^2(\hat{I}(n-k, m-j)) - \hat{\sigma}^2(\hat{I}(n, m))|$$

$$\cdots \tag{1.10}$$

$$V_S[\hat{\sigma}^2(\hat{I})] \equiv \sup_{\substack{n,m \\ (k,j)\in\{1,\ldots,S\}\times\{1,\ldots,S\}}} |\hat{\sigma}^2(\hat{I}(n-k, m-j)) - \hat{\sigma}^2(\hat{I}(n, m))|.$$

---

[a]The model in (1.8) is the natural generalization of classical formulation $T_{\text{noise}}(l) = \sigma_l \cdot \sqrt{2\log(N \cdot M)}$, when noise is assumed to be WSS (see Refs. 10 and 34).

Then, we will prove the following

Theorem 1.1. *Let us consider noise model* (1.1) *and the DDWT implementation given in schemes* 1 *and* 2. *Then, the estimated subband variances* $\hat{\sigma}^2_{d^I}(q, l, I(n, m))$, $\hat{\sigma}^2_a(l, I(n, m))$ *with* $q = \{v, h\}$, $l = 1, \ldots, D$, *are given by*

$$\hat{\sigma}^2_{d^I}(q, l, I(n, m)) = \hat{\sigma}^2(\hat{I}(n, m))\frac{(2^{2(l-1)} + 1)(2^{2l-1} + 1)}{3 \cdot 2^{6(l-1)}}$$

$$+ \sum_{k=1}^{N}\sum_{j=1}^{M}(\hat{\sigma}^2(\hat{I}(n - k, m - j)) - \hat{\sigma}^2(\hat{I}(n, m)))(g_l^T(k, j))^2,$$

$$\hat{\sigma}^2_a(l, I(n, m)) = \hat{\sigma}^2(\hat{I}(n, m))\frac{(2^{2l+1} + 1)^2}{9 \cdot 2^{6l}}$$

$$+ \sum_{k=1}^{N}\sum_{j=1}^{M}(\hat{\sigma}^2(\hat{I}(n - k, m - j)) - \hat{\sigma}^2(\hat{I}(n, m)))(h_l^T(k, j))^2,$$

(1.11)

where $g_l^T(k, j)$ *and* $h_l^T(k, j)$ *are the impulse responses of filters having transfer function* $G_l^T(\omega_v, \omega_h) = G_l^T(\omega_v) \cdot H_{l-1}^T(\omega_h)$ *(or analogously changing* ω_v *and* ω_h*) and* $H_l^T(\omega_v, \omega_h) = H_l^T(\omega_v) \cdot H_l^T(\omega_h)$ *respectively given by* (1.6), *with* $G_l(\omega_q) \equiv G_{l,I}(\omega_q)$, $q \in \{v, h\}$, $l = 1, \ldots, D$. *Moreover, we will show that*

$$\left|\hat{\sigma}^2_{d^I}(q, l, I(n, m)) - \hat{\sigma}^2(\hat{I}(n, m))\frac{(2^{2(l-1)} + 1)(2^{2l-1} + 1)}{3 \cdot 2^{6(l-1)}}\right|$$

$$\leq V_{S_g}[\hat{\sigma}^2(\hat{I})]\frac{(2^{2(l-1)} + 1)(2^{2l-1} + 1)}{3 \cdot 2^{6(l-1)}},$$

(1.12)

$$\left|\hat{\sigma}^2_a(l, I(n, m)) - \hat{\sigma}^2(\hat{I}(n, m))\frac{(2^{2l+1} + 1)^2}{9 \cdot 2^{6l}}\right| \leq V_{S_h}[\hat{\sigma}^2(\hat{I})]\frac{(2^{2l+1} + 1)^2}{9 \cdot 2^{6l}}$$

using definition given in (1.10) *where* S_g *and* S_h *are the support of filters* g_l^T *and* h_l^T *respectively. Moreover, following* (1.11) *and* (1.12), *we are induced to adopt the approximations*

$$\hat{\sigma}^2_{d^I}(q, l, I(n, m)) = \hat{\sigma}^2(\hat{I}(n, m)) \cdot \frac{(2^{2(l-1)} + 1)(2^{2l-1} + 1)}{3 \cdot 2^{6(l-1)}}$$

and

$$\hat{\sigma}^2_a(l, I(n, m)) = \hat{\sigma}^2(\hat{I}(n, m)) \cdot \frac{(2^{2l+1} + 1)^2}{9 \cdot 2^{6l}}.$$

This result allows us to consider a wide class of noise additive models suitable for very different applicative contexts. This turns out to be the right setting in many practical cases. In particular, when low contrast images are considered and DDWT is implemented by a few levels ($D \leq 3$) that are enough to emphasize small objects, then this approximation gives satisfactory simulation results. This is motivated by a low $V_S[\hat{\sigma}^2(\hat{I})]$ and a small support S in these practical cases, recalling the estimates given in (1.11). In Sec. 3, we will provide simulation results to validate this assumption. Finally, we get

Remark 1.1. Results in Theorem 1.1 are used in relation (1.8) in order to provide a direct tuning of denoising threshold given by

$$T_{\text{noise}}(l, \hat{I}(n,m)) = \sqrt{2 \log(N \cdot M)} \cdot \sqrt{\hat{\sigma}^2(\hat{I}(n,m)) \frac{(2^{2(l-1)} + 1)(2^{2l-1} + 1)}{3 \cdot 2^{6(l-1)}}}. \quad (1.13)$$

Note that $T_{\text{noise}}(l, \hat{I}(n,m))$ at level l does not depend on the noise variance at level l, but only on the noise variance estimation $\hat{\sigma}^2(\hat{I}(n,m))$, thus making possible an easy and fast implementation of thresholds selection. In the following sections we will confirm this statement.

Then, the crucial step of denoising is the estimation of term $\hat{\sigma}^2(\hat{I}(n,m))$ that is performed here by a recent and clever algorithm described in Ref. 15. In Sec. 3, we will provide also some results of the whole estimation procedure.

At this point, considering again schemes in Figs. 1 and 3, we can deal with the contrast enhancement operator $E(\cdot)$. It is well known that denoising in mammographic images is necessary to optimize contrast improvement performance. This step is needful to improve image quality and diagnosis capability of radiologists in the case of mammographic images. Consequently, a suitable enhancement operator has to be implemented. In this paper, we consider the operator $E(\cdot)$ defined by

$$E(x) = \begin{cases} 0, & |x| < T_{\text{enh}}, \\ G \cdot (\text{sign}(x)(|x| - T_{\text{enh}})), & |x| > T_{\text{enh}}. \end{cases} \quad (1.14)$$

A hard task in this topic is the choice of T_{enh} and G, which turn out to be crucial in the applications. In respect to previous works,[41,8] here we are able to set the threshold T_{enh} and the gain G as follows:

T_{enh} takes into account residual noise kept by the preliminary denoising procedure. In fact, in order to preserve details that mostly retain information about small cancer signs, denoising procedure cannot be too conservative. Consequently, threshold T_{enh} is computed following an analogous approach as for T_{noise} in operator $D(\cdot)$ that we will describe in the following. Here, it can be important to note that operator $E(x)$ still set to zero small Laplacian coefficients, in contrast with the standard soft-thresholding operators used in literature for contrast enhancement. This fact has been already motivated in step (vi) in Sec. 1.

G is chosen according to considerations made in Sec. 1. In particular, assuming that gradient coefficients at first level contain mostly noise and that microcalcifications are in the second or in the third level according to their dimension, we set $G_1 = 2$, and we set $G_2 + G_3 = \text{const}$. Doing so, we need to choose only G_2 or G_3. This further setting is accomplished by comparing the number of nonzero wavelet coefficients in $(d_{v,l}^{II} + d_{h,l}^{II})$ in levels 2 and 3. The more the information is at level 2 the more G_2 tends to maximum value. G_3 is chosen accordingly. These considerations turn out by a statistical analysis performed over 200 mammographic images containing microcalcifications. In Sec. 3, we will also provide numerical values for G in some practical cases.

Consider now the setting of threshold T_{enh}. As a preliminary result we state that

Theorem 1.2. *Let us consider noise model* (1.1) *and the DDWT implementation given in schemes* 1 *and* 2. *Consider also scheme in Fig.* 3. *Then, the subband variance* $\hat{\sigma}^2_{d^{II}}(q, l, I(n,m))$ *with* $q = \{v, h\}$, $l = 1, \ldots, D$, *is given by*

$$\hat{\sigma}^2_{d^{II}}(q, l, I(n,m)) = \hat{\sigma}^2(\hat{I}(n,m))\frac{(2^{2l}+2)(2^{2l}+5)}{9 \cdot 2^{6(l-1)}} + \sum_{k=1}^{N}\sum_{j=1}^{M}(\hat{\sigma}^2(\hat{I}(n-k, m-j))$$

$$- \hat{\sigma}^2(\hat{I}(n,m)))(g_l^T(k,j))^2 \tag{1.15}$$

where $g_l^T(k,j)$ *is the impulse response of filters having transfer function* $G_l^T(\omega_v, \omega_h) = G_l^T(\omega_v) \cdot H_{l-1}^T(\omega_h)$ *(or analogously changing* ω_v *and* ω_h*) and* $H_l^T(\omega_v, \omega_h) = H_l^T(\omega_v) \cdot H_l^T(\omega_h)$ *respectively given by* (1.6) *with* $G_l(\omega_q) \equiv G_{l,II}(\omega_q)$, $q \in \{v, h\}$, $l = 1, \ldots, D$. *Moreover, we will show that*

$$\left| \hat{\sigma}^2_{d^{II}}(q, l, I(n,m)) - \hat{\sigma}^2(\hat{I}(n,m))\frac{(2^{2l}+2)(2^{2l}+5)}{9 \cdot 2^{6(l-1)}} \right|$$

$$\leq V_{S_g}[\hat{\sigma}^2(I_0)]\frac{(2^{2l}+2)(2^{2l}+5)}{9 \cdot 2^{6(l-1)}} \tag{1.16}$$

where V_{S_g} *is defined as in Theorem* 1.1. *As above, following* (1.15) *and* (1.16)*, we are induced to adopt the approximation*

$$\hat{\sigma}^2_{d^{II}}(q, l, I(n,m)) = \hat{\sigma}^2(\hat{I}(n,m)) \cdot \frac{(2^{2l}+2)(2^{2l}+5)}{9 \cdot 2^{6(l-1)}}. \tag{1.17}$$

The validity is the same as discussed previously.

Later, we will show that the term $\frac{(2^{2l}+2)(2^{2l}+5)}{9 \cdot 2^{6(l-1)}}$ represents the energy of the cascaded filters $|G_l^T(\omega_v, \omega_h)|$ given by Eq. (1.6) with $G_l(\omega_q) \equiv G_{l,II}(\omega_q)$. Finally, using Eqs. (1.15) and (1.16) we have the following remark.

Remark 1.2. Threshold $T_{\text{enh}}(l, \hat{I}(n,m))$ in the contrast enhancement operator $E(\cdot)$, under the assumption of the heteroscedastic noise model described in (1.1) is set to

$$T_{\text{enh}}(l, \hat{I}(n,m)) = \sqrt{2\log(N \cdot M)} \cdot \sqrt{\hat{\sigma}^2(\hat{I}(n,m)) \cdot \frac{(2^{2l}+2) \cdot (2^{2l}+5)}{(9 \cdot 2^{6(l-1)})}} \tag{1.18}$$

where $\hat{\sigma}^2(\hat{I}(n,m))$ is evaluated following the same observations made in the setting of threshold T_{noise}.

By setting the thresholds $T_{\text{noise}}(l, \hat{I}(n,m))$ and $T_{\text{enh}}(l, \hat{I}(n,m))$ using Eqs. (1.13) and (1.18) we provide an efficient procedure within DDWT for denoising and contrast enhancement of low contrast regions with very small cancer signs, thanks to an accurate subband energy evaluation. The main differences among scheme in Fig. 1 and schemes described in Refs. 25 and 24 concern, first of all, the thresholds selection method, that here is directly related to noise power taking into account heteroscedasticity of noise contribution. Secondly, in our work denoising operator $D(\cdot)$ and enhancement operator $E(\cdot)$ are applied directly to wavelet coefficients in each subband separately. In converse, $D(\cdot)$ is usually applied to the modulus of gradient $M_l = \sqrt{(d_{v,l}^I)^2 + (d_{h,l}^I)^2}$ and $E(\cdot)$ to Laplacian coefficients given by $L_l = d_{v,l}^{II} + d_{h,l}^{II}$. As a drawback, considering M_l and L_l, pseudo-inverse filtering operations are needed in order to obtain the two subband matrix coefficients after the processing of M_l and L_l thus introducing computational errors. Moreover, by considering M_l and L_l, the intersubband noise correlation between $d_{h,l}^I$ and $d_{v,l}^I$, and between $d_{h,l}^{II}$ and $d_{v,l}^{II}$ should be evaluated. Finally, recalling that this choice is motivated by the isotropy of L_l and of M_l, note that, in the case of mammographic images, details such as microcalcifications have a very small size so that isotropy is not a crucial property. Moreover, to avoid geometric distortion, we apply the same threshold $T_{\text{noise}}(l, \hat{I}(n,m))$ to $d_{v,l}^I$ and $d_{h,l}^I$ and the same $T_{\text{enh}}(l, \hat{I}(n,m))$ to $d_{v,l}^{II}$, and $d_{h,l}^{II}$.

In the following section we will prove the statements of the main results while in Sec. 3, we will provide results of the application of the proposed algorithm and we will inspect numerical aspects of the method.

2. Proofs of the Main Results

Here below we recall noise model in Eq. (1.1).

$$I(n,m) = I_0(n,m) + \tilde{I}(n,m) = I_0(n,m) + \eta(n,m) \cdot \sigma(I_0(n,m)),$$

with $n = 1, \ldots, N$, $m = 1, \ldots, M$. In order to propagate the noisy contribution $\tilde{I}(n,m)$ through a Linear Shift Invariant (LSI) filter, let us denote with $I_f(n,m)$ the output of a 2D LSI filter having $\tilde{I}(n,m)$ as input and $f(n,m)$ as impulse response. By convolution, we have that $I_f(n,m) = \tilde{I}(n,m) * f(n,m)$. Moreover, we assume separability of used filters, so that in the Fourier domain transfer function $F(\omega_v, \omega_h)$ of the filter corresponds to $F(\omega_v) \cdot F(\omega_h)$. Then, we have the following result.

Lemma 2.1. *The estimated noise variance of the noisy output $I_f(n,m)$ is given by*

$$\hat{\sigma}^2(I_f(n,m)) = \sum_{k=1}^{N}\sum_{j=1}^{M}(f(k,j))^2 \hat{\sigma}^2(\hat{I}(n-k, m-j)). \tag{2.1}$$

Proof. The proof can be easily accomplished by standard arguments from random process theory (see for example Ref. 39) and considering the definition of filters given in Sec. 1. □

As a corollary of Theorem 1.1 and Lemma 2.1, and using again the definition of $V_S[\hat{\sigma}^2(\hat{I})]$, we easily get the following

Corollary 2.1. *With the same notations of Lemma 2.1 and using the definition of $V_S[\hat{\sigma}^2(\hat{I})]$ we also have*

$$\left| \sum_{k=1}^{N}\sum_{j=1}^{M} \hat{\sigma}^2(\hat{I}(n-k,m-j))(f(k,j))^2 - \sum_{k=1}^{N}\sum_{j=1}^{M} \hat{\sigma}^2(\hat{I}(n,m))(f(k,j))^2 \right|$$
$$\leq V_S[\hat{\sigma}^2(\hat{I})] \sum_{k=1}^{N}\sum_{j=1}^{M} (f(k,j))^2.$$

Finally, using Lemma 2.1 and Corollary 2.1, for small values of S, or more generally for small values of $V_S[\hat{\sigma}^2(\hat{I})]$, we may and do assume the following approximation

$$\tilde{\sigma}^2(I_f(n,m)) = \hat{\sigma}^2(\hat{I}(n,m)) \sum_{k=1}^{N}\sum_{j=1}^{M} (f(k,j))^2, \tag{2.2}$$

or equivalently, by Parseval's inequality

$$\tilde{\sigma}^2(I_f(n,m)) = \hat{\sigma}^2(\hat{I}(n,m)) \frac{1}{4(\pi)^2} \int_{-\pi}^{\pi}\int_{-\pi}^{\pi} |F(\omega_v,\omega_h)|^2 \, d\omega_v \, d\omega_h. \tag{2.3}$$

The assumptions in Corollary 2.1 are usually verified in very low contrast images represented by a small range of luminance values such as mammographic images where the gradient of intensity image is locally small owing to the similar absorption characteristics of glandular tissue and tumoral masses. Since noise variance depends on the intensity, if this has a slow variation the same holds for the noise variance. This consideration is strengthened by the fact that filters implementing DDWT have a small support, especially using only three decomposition levels, that are enough to detect and isolate bounded cancer signs such as microcalcifications. Using Lemma 2.1, Corollary 2.1, and results proved in Ref. 34 we are able to prove Theorem 1.1.

2.1. *Proof of Theorem 1.1*

Proof. Using Corollary 2.1 we need to evaluate $\frac{1}{4(\pi)^2} \int_{-\pi}^{\pi}\int_{-\pi}^{\pi} |F(\omega_v,\omega_h)|^2 d\omega_v\omega_h$ in each subband with F given by

$$|F(\omega_v,\omega_h)|^2 = \prod_{k=1}^{l-1} |H_k(\omega_v)|^2 |G_l(\omega_v)|^2 \prod_{r=1}^{l-1} |H_r(\omega_h)|^2$$

with $G_l(\omega_q) = G_l^I(\omega_q)$, $q = \{v, h\}$. By Ref. 34 (Theorem 3.2), it follows that

$$\frac{1}{4(\pi)^2} \int_{-\pi}^{\pi} \int_{-\pi}^{\pi} |F(\omega_v, \omega_h)|^2 \, d\omega_v \, d\omega_h = \frac{(2^{2(l-1)} + 1)(2^{2l-1} + 1)}{3 \cdot 2^{6(l-1)}},$$

ending the proof. $\square$

Using now relations (1.11) and considering again relation (1.8), we finally get

$$T_{\text{noise}}(l, \hat{I}(n, m)) = \sqrt{2 \log(N \cdot M)} \cdot \sqrt{\hat{\sigma}^2(\hat{I}(n, m)) \frac{(2^{2(l-1)} + 1)(2^{2l-1} + 1)}{3 \cdot 2^{6(l-1)}}}, \quad (2.4)$$

that is Remark 1.1 (Eq. (1.13)). Now, let us consider threshold $T_{\text{enh}}(l, \hat{I}(n, m))$ in the contrast enhancement operator $E(\cdot)$. Following above considerations for the setting of the threshold $T_{\text{noise}}(l, \hat{I}(n, m))$, using again Lemma 2.1 and Corollary 2.1, let us prove Theorem 1.2.

2.2. *Proof of Theorem* 1.2

Proof. Applying results of Lemma 2.1 and Corollary 2.1 to $\hat{\sigma}_{d^{II}}^2(q, l, I(n, m))$, with $g_l^T(k, j)$ related to the transfer function $F(\omega_v, \omega_h) = G_l^T(\omega_v)H_{l-1}^T(\omega_h)$ or, by symmetry, $F(\omega_v, \omega_h) = G_l^T(\omega_h)H_{l-1}^T(\omega_v)$ with $G_l(\omega_q) = G_l^I(\omega_q)G_l^{II}(\omega_q)$, we easily get

$$\left| \hat{\sigma}_{d^{II}}^2(q, l, I(n, m)) - \hat{\sigma}^2(\hat{I}(n, m)) \sum_{k=1}^{N} \sum_{j=1}^{M} (g_l^T(k, j))^2 \right| \leq V_S[\hat{\sigma}^2(\hat{I})] \sum_{k=1}^{N} \sum_{j=1}^{M} (g_l^T(k, j))^2.$$

Now, we only need to evaluate the term $\sum_{k=1}^{N} \sum_{j=1}^{M} (g_l^T(k, j))^2$ (i.e. the energy of Laplacian filters) to induce the approximation (1.17). Apply result in Corollary 2.1 with $F(\omega_v, \omega_h)$ given above and using (1.6) we get

$$|F(\omega_v, \omega_h)|^2 = \prod_{k=1}^{l-1} |H_k(\omega_v)|^2 |G_l(\omega_v)|^2 \prod_{r=1}^{l-1} |H_r(\omega_h)|^2. \quad (2.5)$$

Consider now $\prod_{k=1}^{l-1} |H_k(\omega_v)|^2 |G_l(\omega_v)|^2$ and $\prod_{r=1}^{l-1} |H_r(\omega_h)|^2$ separately. Then, applying Eqs. (1.4) and (1.5), by the same arguments used in Ref. 34 (Theorems 3.1 and 3.2) the evaluation of term $\sum_{k=1}^{N} \sum_{j=1}^{M} (g_l^T(k, j))^2$ implies the computation of

$$\frac{16}{2\pi} \int_{-\pi}^{\pi} \frac{\sin^8\left(\frac{2^{l-1}\omega_v}{2}\right)}{2^{4(l-1)} \sin^4\left(\frac{\omega_v}{2}\right)} d\omega_v \cdot \frac{1}{2\pi} \int_{-\pi}^{\pi} \frac{\sin^4\left(\frac{2^{l-1}\omega_h}{2}\right)}{2^{4(l-1)} \sin^4\left(\frac{\omega_h}{2}\right)} d\omega_h.$$

Now, using the same setting of the Proof of Theorem 3.1 in Ref. 34, the Residues theorem and standard algebraic identities, the above integral can be turned into
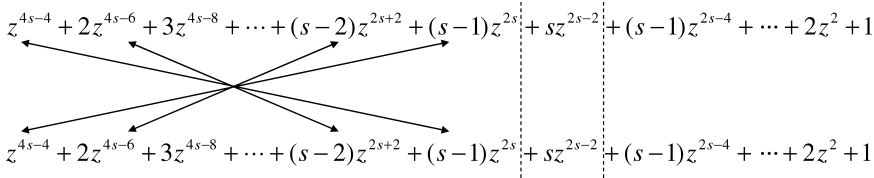
$$z^{4s-4} + 2z^{4s-6} + 3z^{4s-8} + \cdots + (s-2)z^{2s+2} + (s-1)z^{2s} + sz^{2s-2} + (s-1)z^{2s-4} + \cdots + 2z^2 + 1$$

$$z^{4s-4} + 2z^{4s-6} + 3z^{4s-8} + \cdots + (s-2)z^{2s+2} + (s-1)z^{2s} + sz^{2s-2} + (s-1)z^{2s-4} + \cdots + 2z^2 + 1$$

Fig. 4.   Visual evaluation of the terms of order $6s - 4$.

$$z^{4s-4} + 2z^{4s-6} + 3z^{4s-8} + \cdots + (s-1)z^{2s} + sz^{2s-2} + (s-1)z^{2s-4} + \cdots + 3z^4 + 2z^2 + 1$$

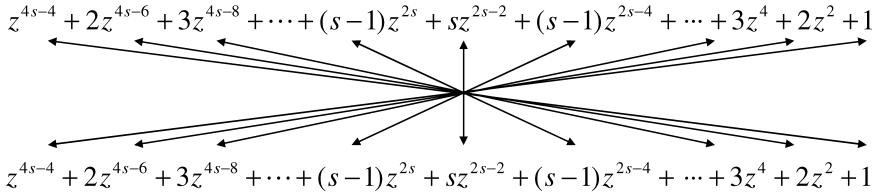$$z^{4s-4} + 2z^{4s-6} + 3z^{4s-8} + \cdots + (s-1)z^{2s} + sz^{2s-2} + (s-1)z^{2s-4} + \cdots + 3z^4 + 2z^2 + 1$$

Fig. 5.   Visual evaluation of the terms of order $4s - 4$.

the following expression

$$-\frac{1}{s^8}\frac{1}{4(\pi)^2}\lim_{z_1 \to 0}\frac{d^{8s-4}}{dz_1^{8s-4}}\left(\left(\sum_{k=0}^{s-1}z_1^{2k}\right)^4(z_1^{2s}-1)^4\right)\cdot\lim_{z_2 \to 0}\frac{d^{4s-4}}{dz_2^{4s-4}}\left(\sum_{r=0}^{s-1}z_2^{2r}\right)^4. \qquad (2.6)$$

Consider now separately the two limits. Referring to Figs. 4 and 5 and using an analogous procedure as in Ref. 34, the reader can easily check that the above integral is equal to

$$\frac{1}{4(\pi)^2}\int_{-\pi}^{\pi}\int_{-\pi}^{\pi}|F(\omega_v, \omega_h)|^2\,d\omega_v\,d\omega_h = \frac{1}{s^8}\left(2\frac{4s^3+5s}{3}\right)\cdot\frac{2s^3+s}{6}$$

and recalling that $s = 2^{l-1}$ we have

$$\frac{1}{4(\pi)^2}\int_{-\pi}^{\pi}\int_{-\pi}^{\pi}|F(\omega_v, \omega_h)|^2\,d\omega_v\,d\omega_h = \frac{(2^{2l}+5)(2^{2l}+2)}{2^{6(l-1)}}$$

that is the thesis.   □

3. Simulation Results and Performance Evaluation

In this section, we experimentally validate the assumptions made in the first part of the paper and provide simulation results of the proposed algorithm. We consider mammographic images taken from Digital Database for Screening Mammography (DDSM)[16,37] and, in particular, we test two classes of ROIs: 187 images containing benign microcalcifications and 160 images containing malignant cluster of microcalcifications. As an example we consider here four images, 12 bpp with a spatial resolution of $43\,\mu$m shown in Fig. 6. The reader can notice that these images have a very low local contrast due to similar absorption characteristics of glandular
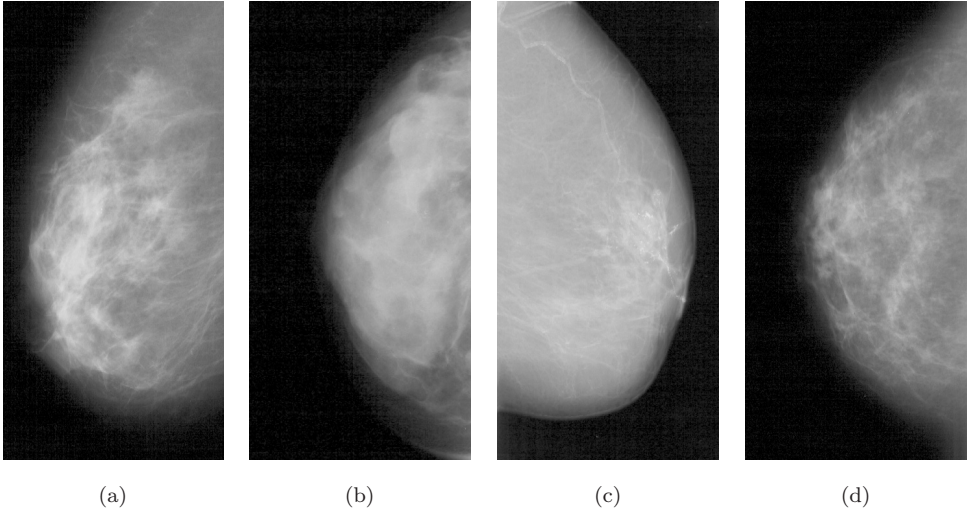
Fig. 6.   Four mammographic images taken from DDSM. Case (a) 1626; (b) 1721; (c) 4132; (d) 1905.

tissue (fibrous and fatty tissue) and cancer signs (massive lesions and microcalcifications), so that masses appear as a part of the tissue itself and microcalcifications are invisible. These images are good representatives of the assumptions we made in Theorems 1.1 and 1.2, since it is acceptable that local variations in the pixel intensity is much smaller than the support of filters involved in the wavelet decomposition, above all because only $D = 3$ levels are needed in order to localize small features with a mean diameter of a few pixels.[b] Firstly, we perform noise variance estimation on these four images, providing a functional relation between noise variance and pixel intensity values.[15,35] An example is shown in Fig. 7 for image in Fig. 6(b). The nonlinear regression performed by the Cubic Smoothing Spline allows us to perform a regression analysis making weak assumptions on the nature of noise affecting the image. In this way, we can take into account different noise contributions simultaneously. Note that noise variance exhibits an evident nonlinear trends with respect to intensity values thus justifying the use of piecewise nonlinear regression. By using this map, we emphasize advantages of using Eqs. (1.11) and (2.2) over the use of relation (2.1) by estimating $\sigma^2(I_0(n,m))$ through the regression curve for every intensity $\hat{I}(n,m)$.[c] Note that the implementation of Eq. (2.1) would not be easy since the square of filters $f(\cdot, \cdot)$ should be evaluated for every subpart of filter bank in Fig. 1 and the convolution with noise variance estimation $\hat{\sigma}^2(\hat{I}(n,m))$

[b]Microcalcifications have a mean diameter in the range [0.1–1] mm so that with a spatial resolution of 50 μm they are represented by [2 ÷ 20] pixels.
[c]Recall that, since we have no $I_0(n,m)$, we build a smoothed version of $I(n,m)$, $\hat{I}(n,m)$ by applying a Gaussian filter to the noisy image $I(n,m)$. Spurious data are anyway eliminated by robust estimators.
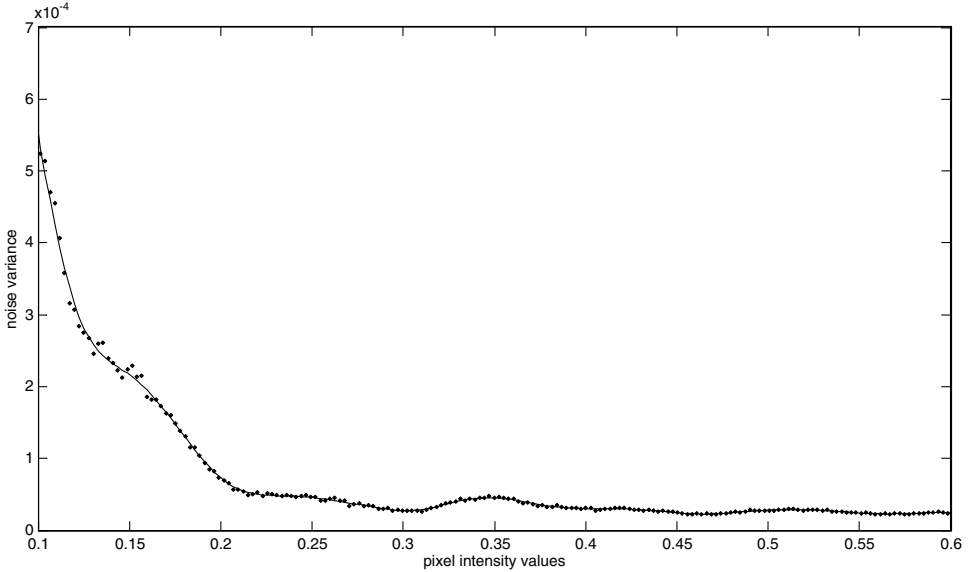
Fig. 7.   An example of a parametric regression analysis by cubic smoothing spline with smoothing parameter $p = 0.99999$ that maps intensity values into noise variance. Case 1721.

should be performed. On the contrary, implementation of Eq. (2.2) is very simple since the energy term is preliminary evaluated, and then only a multiplication by $\hat{\sigma}^2(\hat{I}(n, m))$ is needed. Since both expressions (2.1) and (2.2) tend to zero as decomposition level increases, the discrepancy between the two formulas has to be evaluated carefully. To this aim, we evaluate for every level l a Mean Relative Error (MRE) between the true value $\hat{\sigma}^2_{d^I}(q, l, I(n, m))$ (computed by (2.1)) and its approximation $\tilde{\sigma}^2_{d^I}(q, l, I(n, m))$ (computed by (2.2)). Formally, we have

$$\text{MRE}(l) = \underset{n,m}{\text{mean}} \left(\frac{\hat{\sigma}^2_{d^I}(q, l, I(n, m)) - \tilde{\sigma}^2_{d^I}(q, l, I(n, m))}{\hat{\sigma}^2_{d^I}(q, l, I(n, m))} \right). \tag{3.1}$$

To avoid time consuming, we manually extract from every original mammographic image a Region of Interest (ROI) (see Figs. 8(a1)–8(d1)), i.e. a suspicious region that contains microcalcifications already diagnosed by radiologists. The following simulation results are provided for these ROIs. Note that a ROI's size is variable according to the spatial distribution and the size of microcalcifications that have been already diagnosed by expert radiologists. Evaluating now the MRE for the four ROIs we achieve results in Table 1. Note that, as expected, MRE increases as level increases, because the support S of filter $f(\cdot)$ increases as level increases. Anyway, MRE is smaller than 0.1 so that we can conclude that the difference between the approximated value $\tilde{\sigma}^2_{d^I}(q, l, I(n, m))$ and true value $\hat{\sigma}^2_{d^I}(q, l, I(n, m))$ is much smaller than the actual value itself and consequently approximation in Eq. (2.2) is very good, besides being computationally advantageous.
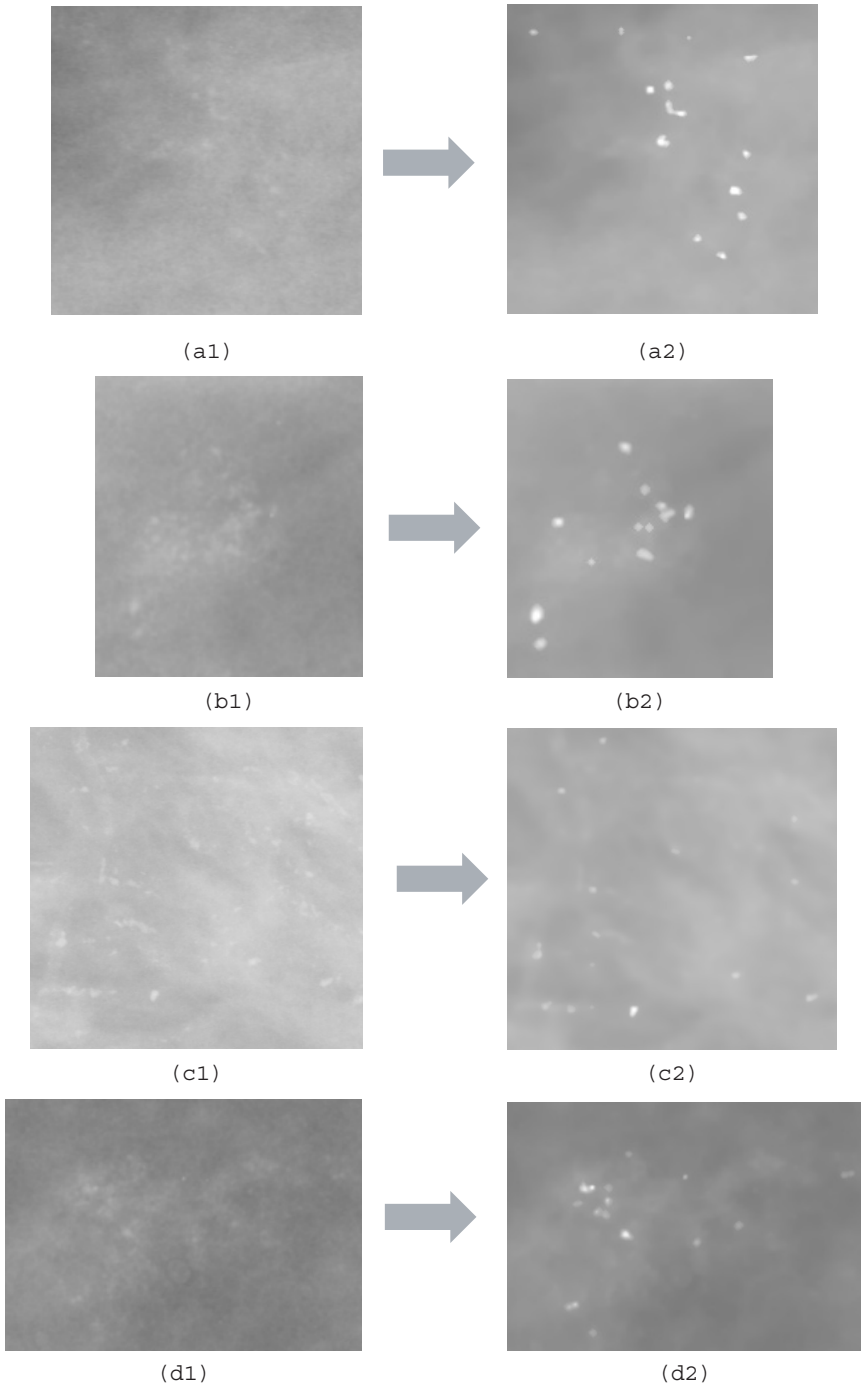
Fig. 8.   Four ROIs containing microcalcifications (a1)–(d1) and the corresponding enhanced versions (a2)–(d2).

Table 1.   MRE vs. level l for the four
ROIs containing microcalcifications.

	Levels		
	$l = 1$	$l = 2$	$l = 3$
Case 1626	0.020	0.048	0.074
Case 1721	0.004	0.012	0.020
Case 4132	0.020	0.050	0.082
Case 1905	0.005	0.015	0.025

Now, we apply denoising and contrast enhancement using the proposed algorithm to the four ROIs. First of all, we show the contents of each decomposition level before and after the application of thresholds. To reduce numbers of figures, we show modulus of gradient M_l and Laplacian L_l. Figures 9(a)–9(d) show contents of three levels for the image in Fig. 6(d). As expected, the first level mostly contains noise, while third level contains tissue and greatest microcalcifications. Usually, second level is the preferred one in order to detect microcalcifications. Anyway, all the three levels maintain certain aspects of the same cancer signs. Figure 11(a) shows instead the approximation matrix $a_3(n, m)$. Note that it does not contain relevant information in order to detect microcalcifications. Anyway, after the reconstruction step, it is emphasized and distorts the final result owing to a final image shrinking. To prevent this effect, we perform the elaboration shown in Fig. 10 and summarized as follows.

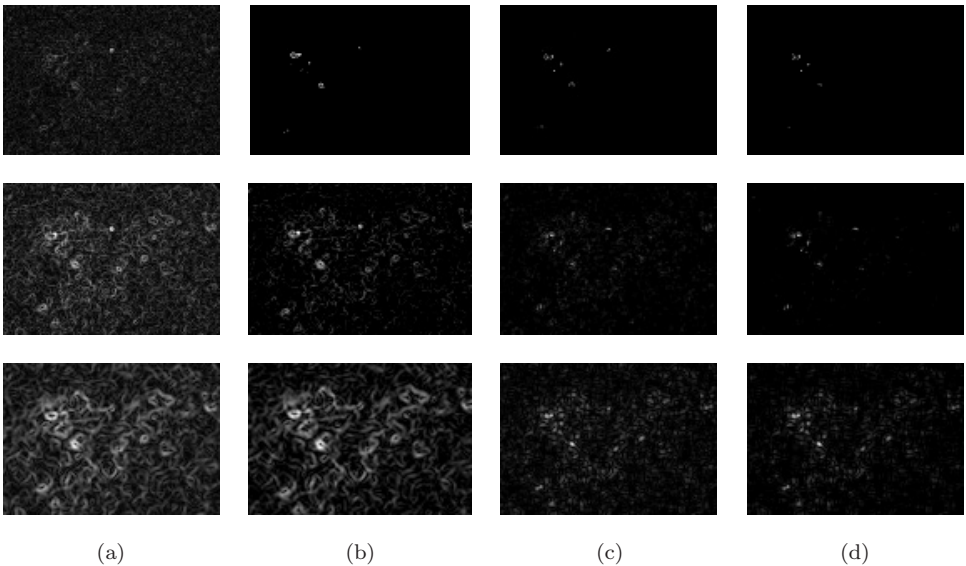|			
(a)	(b)	(c)	(d)

Fig. 9.   Three levels shown for image (d). From top to bottom first — third levels, from left to right before and after denoising, before and after enhancement.
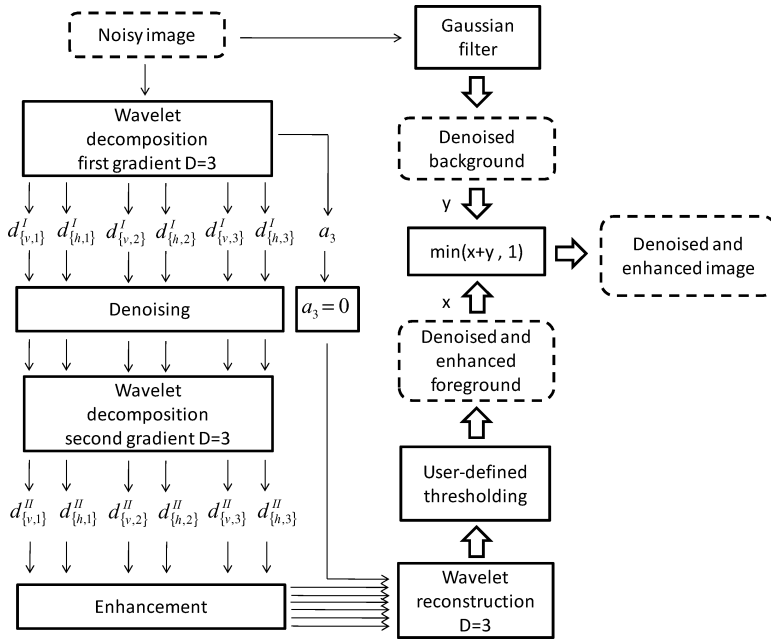
Fig. 10.   A new scheme to separate the denoised background from the denoised and enhanced foreground.

— Perform wavelet decomposition, denoising and enhancement as described above.
— Perform wavelet reconstruction, setting approximation matrix $a_3(n, m)$ to zero.
— Apply a threshold to the reconstructed image maintaining only pixels with the highest luminance, related to microcalcifications. In this way we obtain a denoised and enhanced foreground shown in Fig. 11(b). The thresholding in the pixel domain at this point is mainly motivated by clinical protocol aspects. In fact, the subjectivity of an expert radiologist has to be guaranteed by allowing him to slightly modify the final result by manually applying a threshold on the pixel luminances. In this way, starting from a *keep-all threshold value* the radiologist can reduce the information that are visible on the screen so to add his professional experience to the processed image. The implementation of the thresholding is performed by means of a scroll bar. Later, we will provide some numerical values for this threshold.
— Apply a Gaussian filter to the original image to generate a background image. The result is shown in Fig. 11(c). Note that, there are two main differences between the reconstruction with a nonzero $a_3(n, m)$ and the application of a Gaussian smoothing filter to the original image. First of all, by qualitative results the approximation matrix $a_3(n, m)$ contains details that can confuse the interpretation of the radiologist. So, it is preferred to eliminate it and to recover the smoothed background by applying a Gaussian filter to the original image. Secondly, the background could be recovered by applying only a denoising
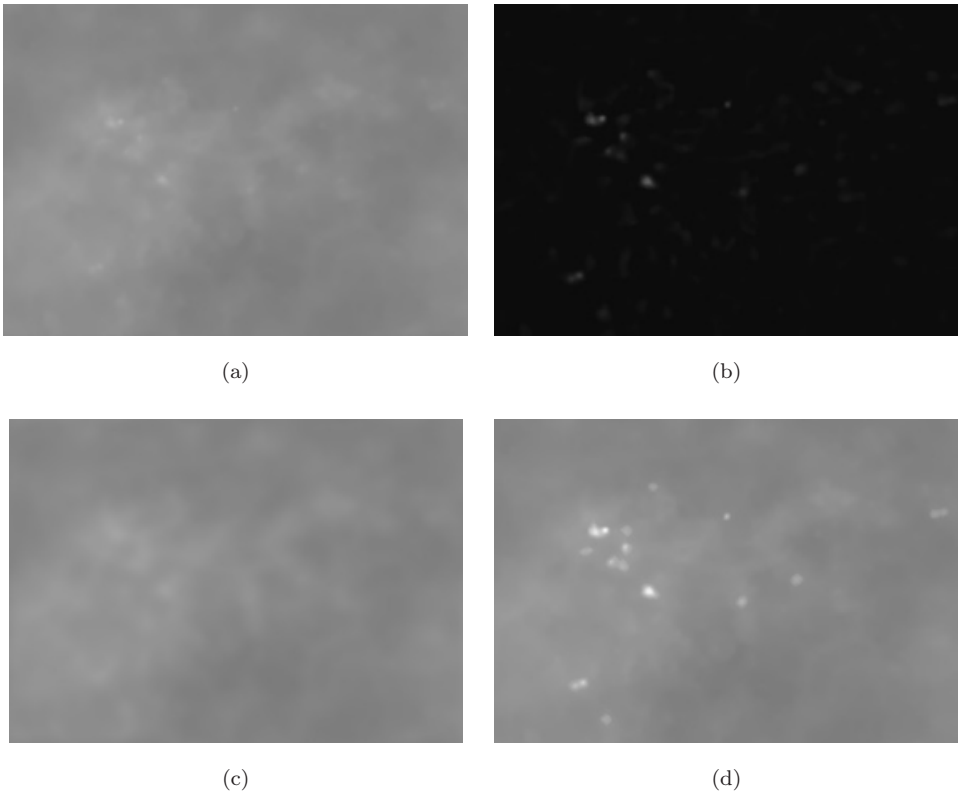
(a)

(b)

(c)

(d)

Fig. 11. (a) Approximation matrix at level three; (b) Recovered denoised and enhanced foreground setting approximation matrix to zero; (c) Denoised background; (d) Bounded sum of images (b) and (c) to preserve original aspect of the image.

procedure by DDWT to the original image, but from computational aspects this is not advantageous.

— Perform a bounded sum of foreground and background to reconstruct an image with the general aspect similar to the original one and with microcalcifications enhanced. The result is shown in Fig. 11(d).

3.1. *Performance evaluation*

The above procedure is also needed to extract from the final image foreground and background. In fact, in order to evaluate the performance of both the denoising and the contrast enhancement procedures, foreground and background of the final image have to be individually compared with foreground and background of the original image.

Now, let us apply the whole denoising and enhancement procedure on the four ROIs shown in Figs. 8(a1)–8(d1). Final results are shown in Figs. 8(a2)–8(d2). Here,

Table 2. Numerical values for vector G and threshold TH in some examples.

ROI	Gains $[G_1, G_2, G_3]$	Threshold TH
Case 1626	[2 30 10]	0.16
Case 1721	[2 30 10]	0.26
Case 4132	[2 10 30]	0.10
Case 1905	[2 20 20]	0.16

the parameters used in the whole enhancement procedure (gain vector $[G_1, G_2, G_3]$ and threshold in the pixel domain TH) are reported in Table 2. Recall that we consider digital images in the normalized range [0, 1]. In addition to the visual inspection of the contrast improvement, in order to evaluate the performance of our algorithm, we compute two indexes: *Contrast Improvement Index* (CII)[25,6] and *Peak Signal-to-Noise Ratio* (PSNR).[28,27] The two indexes evaluate contrast improvement and noise reduction respectively. They are defined as

$$\text{CII} = \frac{C_{\text{Proc}}}{C_{\text{Orig}}}, \quad \text{PSNR} = \frac{p - b}{\sigma_b}$$

where C_{Proc} and C_{Orig} denote contrast in the processed and original image respectively given by

$$C = \frac{f - b}{f + b}$$

where f and b represent the mean gray-level in the foreground and background respectively, p is the maximum gray-level in the foreground, and σ_b is the standard deviation of the background. Obviously, when σ_b is evaluated on the original background it takes into account noise, so that PSNR is smaller for very noisy image. On the contrary, CII takes into account only relative contrast between foreground and background, without considering also noise reduction.

Obviously, the foreground contains details (microcalcifications in this paper) while the background mostly represents glandular tissue. In the proposed method foreground and background are easily achieved by the parallel scheme in Fig. 10. Notice that, if denoising and enhancement are not correctly performed, also residual noise is enhanced and the extraction of f and b cannot be done properly. Figure 12 shows the four masks needed to extract f and b for the considered ROIs. These masks will be then used also for microcalcifications segmentation and features extraction in a classification step. Figure 13 also shows, for a different ROI (case 1248) the effect of contrast enhancement performed on microcalcifications. In particular, a line of the image crossing a microcalcification is plotted for both the original ROI and its enhanced version. The region surrounding the microcalcification is smoothed, since noise is reduced, maintaining the same mean intensity value; moreover, peak referred to the microcalcification is strongly emphasized, thus improving the detection capability of radiologists. Performance evaluation is here reported by the computation of CII and PSNR for 28 images (12 containing malignant cluster of microcalcifications and 16 containing benign microcalcifications). In
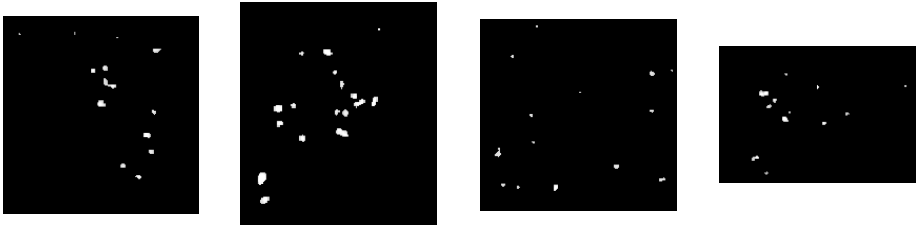
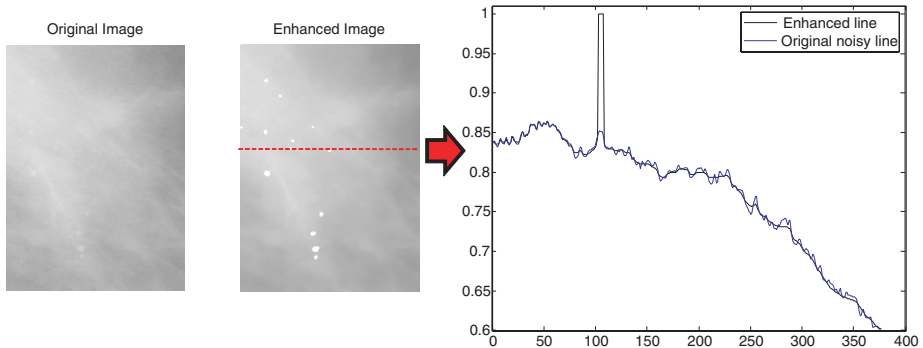Fig. 12.   Masks needed to extract foreground and background.

Fig. 13.   Plotting a line containing a microcalcification for the original image (blue line) and the enhanced version (black line). (Color online.)

particular, we denote with $\text{PSNR}_{\text{Proc}}$, $\text{PSNR}_{\text{Orig}}$, and PSNR_{fin} the PSNR evaluated in the processed ROI, in the original ROI, and the ratio $\text{PSNR}_{\text{Proc}}/\text{PSNR}_{\text{Orig}}$. The images are all taken from DDSM and the DDSM identifier is also inserted in Table 3.[d] In the following, we compare the proposed method for microcalcifications denoising and enhancement with the classical methods *Unsharp Masking* (UM) and *Adaptive Histogram Equalization* (AHE) for the four ROIs in Fig. 8, after a denoising step performed by Wiener filter. Tables 4 and 5 show results for CII and PSNR_{fin} respectively. In particular, we denote with subscripts W the proposed wavelet-based method. The indexes have been evaluated using the same binary mask obtained by the proposed method and a manually set threshold, thus comparing only the contrast achieved in the neighborhood of microcalcifications. Recall that larger values of the indexes mean better enhancement performance. Visual results of the application of the proposed method, UM, and AHE are shown in Fig. 14 for the four ROIs. Beside a quantitative evaluation of the results achieved by the three methods, we also compare them following three criteria.

---

[d]The DDSM identifier contains a letter (A, B, or C) representing a different scanner for the digitalization, the case number, and an acronym identifying the mammographic view used. In particular, L and R stand for left and right breast, while CC and MLO stand for Cranio-Caudal and Medium-Lateral Oblique view.

Table 3.   Result for CII and PSNR for 28 images taken from DDSM.

ROI — Case	C_{Orig}	C_{Proc}	CII	$\text{PSNR}_{\text{Orig}}$	$\text{PSNR}_{\text{Proc}}$	PSNR_{fin}
ROI containing malignant microcalcifications						
$C-0002-1.LCC$	0.062	0.152	2.465	2.839	5.681	2.001
$B-3030-1.RCC$	0.060	0.205	3.431	4.550	13.379	2.940
$B-3082-1.LCC$	0.020	0.114	5.798	2.137	6.687	3.129
$C-0099-1.RCC$	0.052	0.144	2.791	3.655	6.579	1.800
$A-1146-1.LCC$	0.032	0.081	2.551	3.135	8.528	2.721
$A-1213-1.LMLO$	0.064	0.215	3.369	4.508	11.882	2.636
$A-1214-1.LCC$	0.043	0.147	3.410	4.963	12.395	2.497
$A-1220-1.RCC$	0.064	0.177	2.768	6.180	13.558	2.194
$A-1248-1.RMLO$	0.063	0.145	2.287	2.154	3.660	1.699
$A-1469-1.LCC$	0.049	0.277	5.627	2.786	6.913	2.481
$A-1530-1.LMLO$	0.082	0.210	2.557	9.100	17.337	1.905
$A-1538-1.LMLO$	0.015	0.146	9.762	1.527	4.886	3.199
ROI containing benign microcalcifications						
$C-0239-1.LMLO$	0.116	0.310	2.680	3.486	9.200	2.639
$C-0239-1.LCC$	0.107	0.254	2.385	6.492	14.019	2.160
$C-0246-1.LCC$	0.052	0.164	3.165	5.957	13.063	2.193
$B-3104-1.LMLO$	0.058	0.155	2.688	7.568	19.118	2.526
$B-3117-1.RMLO$	0.064	0.153	2.402	3.346	11.743	3.509
$B-3117-1.RCC$	0.032	0.119	3.697	2.512	9.105	3.625
$B-3124-1.RCC$	0.052	0.211	4.015	5.516	21.310	3.863
$B-3131-1.LCC$	0.066	0.159	2.415	5.008	15.824	3.160
$B-3141-1.RMLO$	0.049	0.206	4.198	4.742	13.654	2.879
$B-3145-1.RCC$	0.083	0.216	2.594	2.313	4.664	2.016
$A-1269-1.RCC$	0.028	0.154	5.426	3.234	13.297	4.111
$A-1280-1.LCC$	0.078	0.258	3.312	9.687	24.186	2.497
$A-1285-1.LMLO$	0.045	0.158	3.512	2.761	10.729	3.886
$A-1300-1.LMLO$	0.042	0.091	2.159	4.730	16.254	3.436
$A-1301-1.LCC$	0.048	0.190	3.996	2.268	6.689	2.949
$A-1307-1.LMLO$	0.137	0.321	2.346	5.710	13.138	2.301

Table 4.   Result for CII comparing our method, Unsharp Masking, and Adaptive Histogram Equalization.

ROI — Case	C_{Orig}	C_{W}	CII_{W}	C_{UM}	CII_{UM}	C_{AHE}	CII_{AHE}
Case 1626	0.032	0.113	3.466	0.032	0.978	0.063	1.928
Case 1721	0.040	0.158	3.968	0.039	0.976	0.035	0.870
Case 4132	0.018	0.022	1.199	0.020	1.078	0.049	2.678
Case 1905	0.059	0.162	2.734	0.059	0.992	0.102	1.715

Table 5.   Result for PSNR comparing our method, Unsharp Masking, and Adaptive Histogram Equalization.

ROI — Case	$\text{PSNR}_{\text{Orig}}$	PSNR_{W}	PSNR_{UM}	PSNR_{AHE}
Case 1626	2.130	7.514	1.838	2.976
Case 1721	3.782	11.838	3.350	2.755
Case 4132	3.975	8.797	6.167	3.121
Case 1905	5.062	16.110	4.490	4.867

Proposed enhancement   Unsharp Masking   Adaptive Histogram Equalization

(a)

Proposed enhancement   Unsharp Masking   Adaptive Histogram Equalization

(b)

Proposed enhancement   Unsharp Masking   Adaptive Histogram Equalization

(c)

Proposed enhancement   Unsharp Masking   Adaptive Histogram Equalization
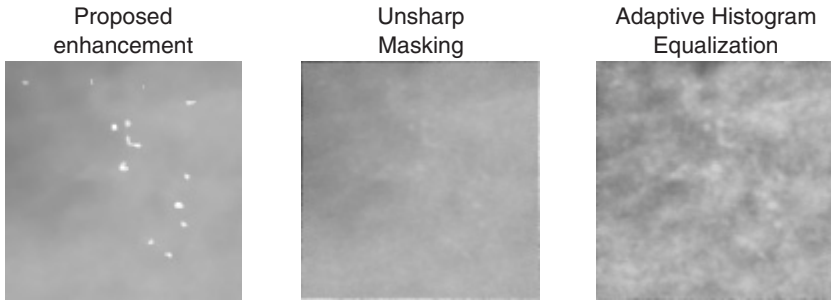
(d)

Fig. 14. Results of contrast enhancement by *Unsharp Masking* and *Adaptive Histogram Equalization*.

— Alteration of the aspect of the original image, thus misleading the interpretation of the image.
— Residual noise.
— Contrast improvement of the important details.

So, note that AHE unacceptably alters the image, especially by the enhancement of the background tissue. Contrast improvement is not localized in the neighborhood of the microcalcifications, but in the whole image. This produces in the case of ROI (c) the highest CII, but also a very low PSNR. On the contrary, UM results appear weak either in residual noise and in contrast improvement (low CII and PSNR for all images) even if the original aspect is maintained. Finally, the proposed method succeeds in preserving the original aspect of the image, emphasizing only regions around microcalcifications according to their shape and size, and moreover reducing noise in the whole image according to the gray-level of each pixel.

4. Conclusion

In this paper, we address the problem of denoising and contrast enhancement of mammographic images by wavelet thresholding using DDWT. It is well known that noise corrupting X-ray images has not a trivial modelization and principally it is signal-dependent. So, assuming a very general noise model, we have firstly applied a robust method in order to estimate noise variance for a heteroscedastic additive noise. Then, we have theoretically derived relations to directly set thresholds either for denoising and for enhancement, specifically for DDWT. The thresholds we propose are both level and noise dependent, according to the assumption that noise amount decreases as level increases and that noise power is strongly influenced by the wavelets filters used. It is also important to underline that the use of DDWT represents a key issue in this context in order to optimize noise reduction, avoiding loss of details and geometric distortion. The method we propose can be applied to many medical images containing small details such as microcalcifications, since simultaneously performs a selective enhancement of small objects and reduces noise according to the gray-value of each pixel, without altering the aspect of the background. This topic is crucial in every Computer Assisted Diagnosis System (CADx) for helping radiologists in an early diagnosis of breast cancer avoiding a misleading or a miss of a tumoral disease.

Acknowledgments

References

1. Practice guideline for digital radiography, Technical Report, ACR American College of Radiology (2007).

2. A. Azzalini, M. Farge and K. Schneider, Nonlinear wavelet thresholding: A recursive method to determine the optimal denoising threshold, *Appl. Comput. Harmon. Anal.* **18**(2) (2005) 177–185.

3. K. Berkner and Jr. R. O. Wells, Smoothness estimates for soft-threshold denoising via translation-invariant wavelet transforms, *Appl. Comput. Harmon. Anal.* **12**(1) (2002) 1–24.

4. H. P. Chan, C. J. Vyborny, H. MacMahon, C. E. Metz, K. Doi and E. A. Sickles, Digital mammography: ROC studies of the effects of pixel size and unsharp-mask filtering on the detection of subtle microcalcifications, *Investigative Radiology* **22**(7) (1987) 581–589.

5. H. Cheng, Y. Lui and R. Freimanis, A novel approach to microcalcification detection using fuzzy logic technique, *IEEE Trans. Med. Imag.* **17**(3) (1998) 442–450.

6. H.-D. Cheng, Computer-aided detection and classification of microcalcifications in mammograms: A survey, *Pattern Recogn.* **36**(12) (2003) 2967–2991.

7. D. Cho, T. D. Bui and G. Chen, Image denoising based on wavelet shrinkage using neighbor and level dependency, *Int. J. Wavelets Multiresolut. Inf. Process.* **7**(3) (2009) 299–311.

8. L. Costaridou, P. Sakellaropoulos, S. Skiadopoulos and G. Panayiotakis, *Medical Image Analysis Methods* (Taylor & Francis, 2005). Chapter 6, Locally Adaptive Wavelet Contrast Enhancement.

9. A. P. Dhawan, G. Buelloni and R. Gordon, Enhancement of mammographic features by optimal adaptive neighborhood image processing, *IEEE Trans. Med. Imag.* **5**(1) (1986) 8–15.

10. D. Donoho, De-noising by soft-thresholding, *IEEE Trans. Inform. Theory* **41**(3) (1995) 613–627.

11. D. L. Donoho and I. M. Johnstone, Ideal spatial adaptation by wavelet shrinkage, *Biometrika* **81** (1994) 425–455.

12. D. L. Donoho, I. M. Johnstone, G. Kerkyacharian and D. Picard, Wavelet shrinkage: Asymptopia? *J. R. Stat. Soc. Ser. B Stat. Methodol.* **57**(2) (1995) 301–369.

13. J. Fan and A. Laine, *Wavelets in Medicine and Biology* (CRC Press, 1996), pp. 163–192.

14. R. Gordon and R. M. Rangayyan, Feature enhancement of film mammograms using fixed and adaptive neighborhoods, *Appl. Opt.* **23**(4) (1984) 560–564.

15. P. Gravel, B. Gilles and J. A. De Guise, A method for modeling noise in medical images, *IEEE Trans. Med. Imag.* **23**(10) (2004) 1221–1232.

16. M. Heath, K. W. Bowyer, D. Kopans, R. Moore and P. Kegelmeyer, *Digital Mammography* (Kluwer Academic Publishers, 1998), pp. 457–460.

17. P. Heinlein, J. Drexl and W. Schneider, Integrated wavelets for enhancement of microcalcifications in digital mammography, *Med. Imag. IEEE Trans.* **22**(3) (2003) 402–413.

18. Z. Huang, B. Fang, X. He and L. Xia, Image denoising based on the dyadic wavelet transform and improved threshold, *Int. J. Wavelets Multiresolut. Inf. Process.* **7**(3) (2009) 269–280.

19. M. Jansen and A. Bulthool, Multiple wavelet threshold estimation by generalized cross validation for images with correlated noise, *IEEE Trans. Image Process.* **8** (1999) 947–953.

20. I. M. Johnstone and B. W. Silverman, Wavelet threshold estimators for data with correlated noise, *J. R. Stat. Soc. Ser. B Stat. Methodol.* **59** (1997) 319–351.

21. N. Karssemeijer, Adaptive noise equalization and image analysis in mammography, in *Information Processing in Medical Imaging: 13th International Conference, IPMI1993*, Arizona, USA (1993), pp. 472–486.

22. A. Khare, U. S. Tiwary and M. Jeon, Daubechies complex wavelet transform based multilevel shrinkage for deblurring of medical images in presence of noise, *Int. J. Wavelets Multiresolut. Inf. Process.* **7**(5) (2009) 587–604.

23. A. Khare and U. S. Tiwary, Soft-thresholding for denoising of medical images. A multiresolution approach, *Int. J. Wavelets Multiresolut. Inf. Process.* **3**(4) (2005) 477–496.

24. A. Laine, J. Fan and W. Yang, Wavelets for contrast enhancement of digital mammography, *IEEE Eng. Med. Biol. Mag.* **14**(5) (1995) 536–550.

25. A. F. Laine, S. Schuler, J. Fan and W. Huda, Mammographic feature enhancement by multiscale analysis, *IEEE Trans. Med. Imag.* **13**(4) (1994) 725–740.

26. M. R. Leadbetter, G. Lindgren and H. Rootzen, *Extremes and Related Properties of Random Sequences and Processes* (Springer-Verlag, New York, USA, 1983).

27. H. Li, K. J. R. Liu and S. C. B. Lo, Fractal modeling of mammogram and enhancement of microcalcifications, in *Nuclear Science Symposium & Medical Imaging Conference*, Vol. 3, Anaheim, California, USA (1996), pp. 1850–1854.

28. H. Li, K. J. R. Liu and S. C. B. Lo, Fractal modeling and segmentation for the enhancement of microcalcifications in digital mammograms, *IEEE Trans. Med. Imag.* **16**(6) (1997) 785–798.

29. S. Mallat, *A Wavelet Tour of Signal Processing* (Academic Press, 1998).

30. S. Mallat and W. L. Hwang, Singularity detection and processing with wavelets, *IEEE Trans. Inform. Theory* **38**(2) (1992) 617–643.

31. S. Mallat and S. Zhong, Characterization of signals from multiscale edges, *IEEE Trans. Pattern Anal. Mach. Intell.* **14**(7) (1992) 710–732.

32. M. B. McSweeney, P. Sprawls and R. L. Egan, Enhanced image mammography, Technical report 140, AJR (1983).

33. A. Mencattini, G. Rabottino, S. Salicone and M. Salmeri, Uncertainty modeling and propagation through RFVS for the assessment of CADx systems in digital mammography, to appear in *IEEE Trans. Instrum. Meas.*

34. A. Mencattini, M. Salmeri, F. Caselli, B. Sciunzi and R. Lojacono, Subband variance computation of homoscedastic additive noise in discrete dyadic wavelet transform, *Int. J. Wavelets Multiresolut. Inf. Process.* **6**(6) (2008) 895–906.

35. A. Mencattini, M. Salmeri, R. Lojacono and M. Arnò, Noise estimation in mammographic images for adaptive denoising, in *EFOMP European Conference on Medical Physics*, Castelvecchio Poscoli, Italy (2007), 2 pp.

36. W. M. Morrow, R. B. Paranjape, R. M. Rangayyan and J. E. L. Desautels, Region-based contrast enhancement of mammograms, *IEEE Trans. Med. Imag.* **11**(3) (1992) 392–406.

37. University of South Florida Digital Mammography Home Page; html://marathon. csee.usf.edu/Mammography/Database.html.

38. V. Oktem and I. Jouny, Automatic detection of malignant tumors in mammograms, in *Conf. Proc. IEEE Eng. Med. Biol. Soc.* **3** (2004) 1770–1773.

39. A. Papoulis, *Probability, Random Variables, and Stochastic Processes*, McGraw-Hill Series in Electrical Engineering, 3rd edn. (McGraw-Hill, 1991).

40. J. Portilla and E. P. Simoncelli, Image denoising via adjustment of wavelet coefficient magnitude correlation, in *Proceedings of the 7th Int. Conf. Image Proc.*, Vancouver, Canada (2000), pp. 402–406.

41. P. Sakellaropoulos, L. Costaridou and G. Panayiotakis, A wavelet-based spatially adaptive method for mammographic contrast enhancement, *Phys. Med. Biol.* **48** (2003) 787–803.

42. J. Salvado and B. Roque, Detection of calcifications in digital mammograms using wavelet analysis and contrast enhancement, in *2005 IEEE International Workshop on Intelligent Signal Processing* (IEEE Press, 2005), pp. 200–205.
43. R. N. Strickland and H. I. Hahn, Wavelet transforms for detecting microcalcifications in mammography, in *Proceedings of the International Conference on Image Processing*, Austin, Texas, USA (1994), pp. 402–406.
44. R. N. Strickland and H. I. Hahn, Wavelet transform for detecting microcalcifications in mammograms, *IEEE Trans. Med. Imag.* **15**(2) (1996) 218–229.
45. R. N. Strickland and H. I. Hahn, Wavelet transform methods for object detection and recovery, *IEEE Trans. Image Process.* **6** (1997) 724–735.
46. M. Unser, A. F. Laine and A. Aldroubi, Wavelets on medical imaging, *IEEE Trans. Med. Imag.* **22**(3) (2003) 285–288.
47. M. Wirth, M. Fraschini and J. Lyon, Contrast enhancement of microcalcifications in mammograms using morphological enhancement and non-flat structuring elements, in *Proc. 17th IEEE Symposium on Computer-Based Medical Systems, CBMS 2004*, Maryland, USA (2004), pp. 134–139.
48. H. Yoshida, K. Doi and R. M. Nishikawa, Automated detection of clustered microcalcifications, in *SPIE Image Processing*, Vol. 2167, Newport Beach, California, USA (1994), pp. 868–886.
49. H. Yoshida, W. Zhang, W. Cai, K. Doi, R. M. Nishikawa and M. L. Giger, Optimizing wavelet transform based on supervised learning for detection of microcalcifications in digital mammograms, in *Proceedings of the IEEE International Conference on Image Processing*, Vol. 3, Washington, DC, USA (1995), pp. 152–155.
50. X. P. Zhang and M. D. Desai, Segmentation of bright targets using wavelets and adaptive thresholding, *IEEE Trans. Image Process.* **10**(7) (2001) 1020–1030.